Influence of Wind on Stratification and Mixing in Mobile Bay, Alabama, a Wide Microtidal Estuary

Zhilong Liu,[a,b] Brian Dzwonkowski,[a,b] John Lehrter,[a,b] , Lisa Lowe,[c] and Jeff Coogan,[d]

[a] *Dauphin Island Sea Laboratory, Dauphin Island, AL, 36528*

[b] *School of Marine and Environmental Sciences, University of South Alabama, Mobile, AL, 36688*

[c] *North Carolina State University, Raleigh, NC, 27695*

[d] *Woods Hole Oceanographic Institution, Woods Hole, MA 02543*

Corresponding author: Zhilong Liu, zliu@disl.org

ABSTRACT

Extensive research has shown that wind has a strong influence on estuarine circulation and salt transport. However, the response to wind forcing in estuarine systems presents challenges due in part to the complexities of realistic forcing conditions, system states, and geomorphologies. To further advance the understanding of estuarine responses to wind forcing, a comprehensive analysis of stratification and mixing during a typical southeast wind event was conducted in Mobile Bay, a microtidal, wide, shallow, and river-dominated estuary in the northern Gulf of Mexico. An analysis of the vertical salinity variance and its associated budget terms shows that the system generally becomes less stratified and fully mixed across much of the system; however, there was significant spatial heterogeneity in physical processes driving the evolution of the water column stratification over the course of the event. Surprisingly, in some regions of the bay, dissipation of salinity variance was secondary to contributions from straining and advection. Furthermore, local wind stress and remote wind driven Ekman transport affected stratification responses and their relative impacts varied spatially across the estuary. Direct turbulent mixing from local wind stress and straining dominated the stratification responses away from the main tidal inlet where estuarine-shelf exchange (i.e., current velocity structure and advection of salinity) from Ekman transport controlled the vertical mixing. This detailed case study highlights the complexity of wind influences in a system like Mobile Bay, a representative typical of the northern Gulf of Mexico and other coastal region.

SIGNIFICANCE STATEMENT

A typical wind event with southeast wind up to 8 m s^{-1} dramatically reduced stratification in Mobile Bay by mixing the north half of the bay while maintaining weak stratification across the west half of the lower bay. Both local wind stress and remote wind driven transport affected stratification inside the bay by reversing the subtidal flow structure and promoting shelf-to-bay salt transport. Local wind stress dominated the stratification responses away from the tidal inlet while estuarine-shelf interaction driven by Ekman transport controlled vertical mixing near the inlet.

1. Introduction

Weather scale meteorological conditions, such as wind stress, can control estuary dynamics by impacting residual velocities and salinity distribution (Weisberg 1976; Wong and Garvine 1984, Ralston et al. 2008, Li and Li 2011). Such forcing can modify estuarine circulation which also controls material transport thought horizontal advection and vertical mixing. The transport and mixing, in turn, affects flushing times and stratification which potentially impacts water quality due to stressors such as hypoxia (Scully 2016, Testa et al. 2017, Zhang et al. 2019). Therefore, investigating how wind modulates estuarine flow structure, salt transport, stratification, and mixing could improve our understanding of both physical and biogeochemical processes in estuarine environments.

Wind impacts estuarine stratification through wind stress, direct wind mixing, and remote wind effects modifying water levels at the coast. Wind stress acting as a surface forcing modulates subtidal gravitational circulation (Wang 1979, Geyer 1997, Burchard 2009) as well as salinity intrusion (Ralston et al. 2008; Coogan and Dzwonkowski, 2018). Typically, the response is highly dependent on the prevailing wind direction. Down-estuary wind enhances estuarine circulation and strains the density gradient stratifying the water column, termed ‘wind straining’ (Scully et al. 2005). While up-estuary wind reduces or even reverses the circulation, thus tends to decrease stratification.

Regardless of direction, wind stress always intensifies turbulence in the upper water column, known as direct wind mixing, resulting in a surface boundary layer and reduced stratification. Under up-estuary wind the direct mixing and negative wind straining (i.e., vertically tilting isopycnals) contribute to reducing stratification (Chen and Sanford 2009, Coogan and Dzwonkowski 2018). Under down-estuary wind, the modification of stratification depends on the competition between direct mixing and positive wind straining (i.e., horizontally tilting isopycnals). As down-estuary wind speeds increase, mixing and the surface boundary layer grows, eventually overcoming straining and are typically associated with storm events (Goodrich et al. 1987, Li et al. 2007, Burchard 2009, Chen and Sanford 2009). Furthermore, remote wind generated coastal Ekman setup can drive barotropic exchange at the mouth (Wong and Moses-Hall 1998, Wong and Valle-Levinson 2002). This remote wind-induced barotropic setup in conjunction with the local wind effect causes significant variability in circulation patterns inside estuaries and further modifies salt intrusions, particularly during large storms (Ralston et al. 2008).

Many previous studies have focused on the impacts of axial wind on stratification in elongated estuaries, where estuary length is much larger than the width. Wind influences in 'wide' systems, where length and width are similar in magnitude, have not been adequately addressed. Systems under realistic wind conditions will deviate from idealized expectations due to wind and estuary direction misalignment, spatial variability in density gradients, and complex geomorphology (e.g., flow constraints like shoal-channel bathymetry and/or relatively narrow tidal inlets). This work aims to quantify the effects of realistic non-axial wind on stratification in a non-elongated, shallow, river-dominated estuary, i.e., Mobile Bay.

In Mobile Bay, wind forcing plays an important role in modifying bay-wide stratification, subtidal exchange, and flushing characteristics. Wind events are a critical component of the subtidal stratification cycles that characterized the dynamics of the bay (Schroeder et al. 1990, Noble et al. 1996, Park et al. 2007, Coogan et al. 2020). Typically, up-estuary wind inhibits exchange and flushing while down-estuary wind enhances exchange and flushing (Du et al. 2018, Coogan and Dzwonkowski 2018). Furthermore, estuary-shelf connectivity can be strongly modified by wind forcing. Kim and Park (2012) found significant temporal variability in the water and salt exchanges occurring at the tidal inlets due to wind forcing. Coastal upwelling and downwelling can also change the hydrographic conditions inside the bay (Cambazoglu et al. 2017, Coogan et al. 2019). This study uses high resolution numerical modeling to observe the interplay of stratification and mixing in response to wind forcing with a particular emphasis on the spatial heterogeneity in stratification across the bay and the associated importance of wind straining, wind mixing, and remote wind effects.

2. Methods

a. Study area

Mobile Bay is a large shallow estuary that links the Mobile-Tensaw River Delta to the northern Gulf of Mexico. The system is a flat, shallow bay (average depth 3 m) in a bar-built drowned valley with an along-axis of 48 km and an across-axis width ranging from 14 – 34 km. Its wide, flat shoals are incised by multiple anthropogenic channels (Fig. 1). The main shipping channel, which is 14 -16 m deep and 280 m wide, generally runs north to south along bay's axis. The Gulf Intracoastal Waterway (3.7 m deep) and a connect to an industrial canal (13 – 14 m deep) both run east to west in southern and middle regions of the bay, respectively. Adding to the bathymetric complexity of the system, Mobile Bay connects to the Gulf through

two narrow tidal inlets, where on average 64% of the exchange between the bay and gulf directly passes through the Main Pass, while the remaining 36% passes through Pass Aux Herons to Mississippi Sound (Kim and Park, 2012).

Mobile Bay is classified as a microtidal, stratified, river-dominated system. The diurnal tidal constituents are dominant with a fortnightly tidal range that varies from 0.0 – 0.8 m due to tropical equitization (Seim et al. 1987). The tropic– equatorial cycle (13.66 days) is a result of the interaction of the K1- O1 tidal constituents (Kim and Park 2012). The average river discharge to the estuary is 1,866 $m^3 s^{-1}$ over the 1930 – 2019 period and has significant seasonal variations (Dykstra and Dzwonkowski 2021). Wind patterns also show distinct seasonal variation, where southerly wind is dominant in spring and summer, and stronger northerly wind is dominant in fall and winter (Noble et al. 1996).

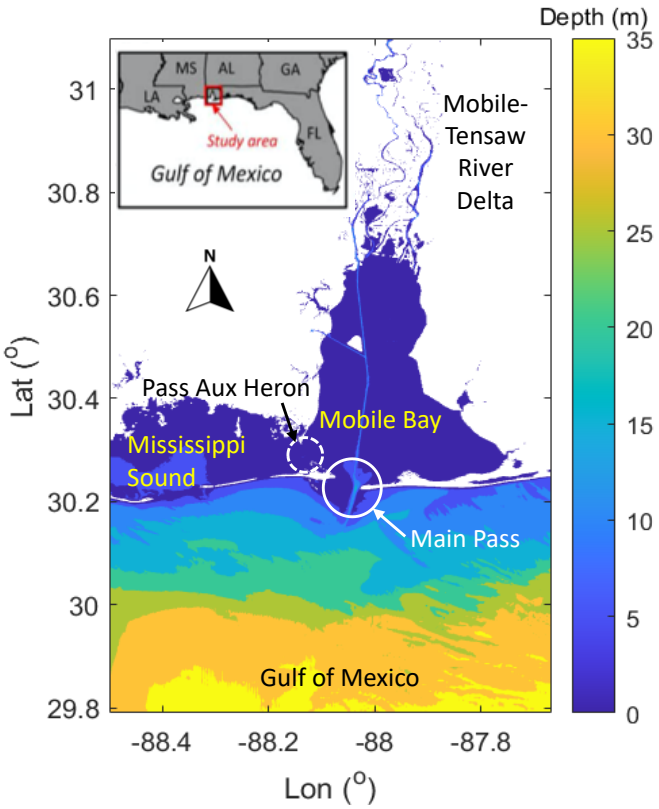

Fig. 1 Map of Mobile Bay as represented by the ROMS model domain with color contours denoting bathymetry. Circles with arrows denotes tidal inlets. The insert in the top left corner shows the study area in context to the broader northern Gulf of Mexico.

b. Hydrodynamic model

In this study, we developed a three-dimensional model of Mobile Bay based on the Regional Ocean Modeling System (ROMS). The model covers the delta, Mobile Bay, and part of Mississippi Sound and nearby coastal region with a range from 87.67° - 88.50° W (80.37 km) and 29.79° - 31.09 °N (144.60 km, Fig. 1). The mesh was built with bathymetry and topography data from Mobile, Alabama 1/3 arc-second NAVD 88 Coastal Digital Elevation Model (NOAA National Geophysical Data Center, 2009), of which the horizontal resolution was around 8.87 m in the longitudinal direction and 10.27 m in the latitudinal direction (Amante et al. 2011). Additional data from 112 hydrographic surveys between 2012 and 2019 from the Army Corps of Engineers eHydro Survey Data portal (geospatial usace.opendata.arcgis.com/datasets/80a394bae6b547f1b5788074261e11f1_0) were used to provide the latest bathymetry in Mobile River, Tombigbee River, and the associated shipping channel.

The model domain has 600 grid cells in the east-west direction, 840 grid cells in the north-south direction, and 16 layers in the vertical direction with near-surface and near-bottom refinement. A horizontally varying grid was used to resolve the complexity of the system, where the grid size is 70 - 90 m in the delta, shipping channel, and tidal inlets. There is a gradual increase to 250 - 430 m towards the open boundaries. The wet/dry option was turned on with truncated topography up to 1.0 m above sea level.

The model was forced by both hydrodynamic and meteorological variables. The tidal elevation forcing was mapped from the Western North Atlantic, Caribbean and Gulf of Mexico ADCIRC Tidal Databases including diurnal (K1, O1, Q1), semidiurnal (M2, S2, N2, K2) and over-tide constitutes (M4, M6). Hourly non-tidal water level and currents, temperature, and salinity were applied at the open (western, southern, and eastern) boundaries using data obtained from the Northern Gulf of Mexico Operational Forecast System (NGOFS, Wei et al., 2014; Zheng et al., 2020). River discharge was applied at the closed northern boundary by summing up discharge data at the Alabama River (USGS 02428400), Tombigbee River (USGS 02469761) and Satilpa Creek (USGS 02469800) stations. Meteorological forcing, including 3-hourly solar radiation, precipitation, wind, air temperature, sea surface temperature and humidity, was obtained from the National Centers for Environmental Prediction (NCEP)'s North American Regional Reanalysis (NARR) data. The net heat flux was corrected to eliminate differences between modeled sea surface temperature to prescribed sea surface

temperature (Barnier et al. 1995) by turning on "QCCORRECTION" option in ROMS. The model was initialized with no flow and a flat sea surface and has three-dimensional temperature and salinity mapped from NGOFS's outputs. A 2-day tidal ramp-up was applied at the start of simulations.

Wind imposes momentum directly through wind stress and intensifies turbulence at the water surface. Wind stress (τ_w) is computed based on air density (ρ_a), drag coefficient (C_D) and imposed wind speed at 10 m above sea level(U_{10}) following a typical quadratic relationship: $\tau_w = \rho_a C_D {U_{10}}^2$. By assuming the wind profile followed a logarithmic law, the drag coefficient C_D is related to the Von Karman constant κ (= 0.4) and surface roughness z_0^a: $C_D = \kappa^2 / \left[ln\left(\frac{10}{z_0^a}\right)\right]^2$. The dependence of the surface roughness to wind speed is $z_0^a = \alpha_a u_a^{*2}/g$ (Charnock 1955), where u_a^* is the friction velocity defined as $u_a^{*2} = C_D {U_{10}}^2$, g is gravitational acceleration, and α_a is Charnock coefficient. Therefore, once α_a is determined the parameterization of C_D is closed. In ROMS, the standalone hydrodynamic model adopts a bulk wind speed dependent α from Taylor and Yelland (2001) where $\alpha_a = 0.011$ when $U_{10} \leq$ 10 m s^{-1}; $\alpha_a = 0.018$ when $U_{10} \geq 18$ m s^{-1}; α_a linearly increases from 0.011 to 0.018 when $10 < U_{10} < 18$ m s^{-1}. Explicit wave impacts on α_a and C_D were not considered in this work.

Besides imposing a momentum flux, wind forcing also modifies ocean surface turbulence by changing the surface friction velocity u_w^* and roughness length z_0^w on the water side of the air-sea interface. Surface friction velocity directly links to wind stress τ_w, i.e., $u_w^* = \sqrt{\tau_w/\rho_w}$, where ρ_w is water density. Water side roughness length z_0^w can be parameterized as a Charnock-type relationship $z_0^w = \alpha_w u_w^{*2}/g$ (Bye 1988). Churchill and Csanady (1983) suggested α_w = 1, 400 according to near-surface measurements. In the presence of waves, z_0^w should be parameterized as a linear function of significant wave height i.e., $z_0^w = \alpha_{hs} H_{sig}$ (Terray et al. 1996). Since wave forcing was not included in this work, by following common practice (Paskyabi and Fer 2014), a constant value α_w = 1, 400 was used in this work.

A third-order upstream scheme and fourth-order centered scheme were used for horizontal and vertical advection of the 3D momentum, respectively. Tracer (salinity and temperature) advection utilizes multidimensional positive definite advection transport algorithm (MPDATA, Smolarkiewicz and Margolin, 1998) since water temperature is always positive in Mobile Bay. The generic $k-\varepsilon$ turbulence closure scheme (Umlauf and Burchard 2003; Warner et al. 2005) was used with background vertical viscosity and diffusivity set at 1×10^{-5} m^2 s^{-1}

and 1×10^{-6} m^2 s^{-1} respectfully. The horizontal eddy viscosity and diffusivity were set at 0.1 m^2 s^{-1}. Logarithmic bottom friction is used under the assumption that the bottom boundary layer is logarithmic with a roughness height of 5 mm. This model configuration allowed for a maximum time step of 3 seconds. We conducted a yearlong simulation with hourly records of model outputs for 2019 by starting from November 2018, which allowed for a two month ramp up of the model.

c. Vertical salinity variance

Stratification was measured by vertical salinity variance (Burchard and Rennau 2008; Burchard et al. 2009; Wang et al. 2017; MacCready et al. 2018). The budget equation for the water column integrated salinity variance [Eq. (1), Li et al., 2018] is

$$\frac{\partial \int S'^2 dz}{\partial t} = -\nabla_h \int \boldsymbol{u}_h S'^2 dz + \int -2\boldsymbol{u}' S' \cdot \nabla_h \bar{S} dz - \int 2K_z \left(\frac{\partial S'}{\partial z}\right)^2 dz, \qquad (1)$$

where the salinity variance, $S'^2 = (S - \bar{S})^2$, is the squared deviation of salinity (S) relative to the depth average value ($\bar{S}$), $\boldsymbol{u}_h$denotes the horizontal velocity vector, $\boldsymbol{u}'$ is the deviation of horizontal velocity vector from the depth average value, K_z is the vertical eddy diffusivity and ∇_h is the horizontal differential operator.

In Eq. (1), the term on the left-hand side is salinity variance tendency. It denotes the local increase or decrease of vertical salinity variance with respect to time. The terms on the right-hand side are advection, straining, and dissipation, respectively. The advection term including the negative sign denotes salinity variance being transported into (i.e., convergence, positive value) or out of (i.e., divergence, negative value) the local region. Straining denotes the conversion between horizontal variance and vertical variance, which is the titling of isohalines by vertical differences in salt advection. Positive straining corresponds to a stratifying water column when advection tends to move fresher water over saltier water. The dissipation term is always positive so that the negative of this term reduces salinity variance indicating that vertical mixing always destroys stratification. In the data analysis, depth-average vertical salinity variance $\overline{S'^2}$ and each budget term in Eq. (1) were calculated from hourly model outputs. A low-pass 48-hr Lanczos filter was applied to $\overline{S'^2}$ and the associated budget terms to remove tidal signals and isolate the subtidal changes from other forcings, namely wind.

3. Results

Outputs of the three-dimensional flow field and hydrography were used to explore the impact of a wind event on stratification during the early summer season. Early summer is a period when the prevailing winds in the northern Gulf of Mexico transition from northerlies to southerlies (Noble et al. 1996). During the summer, the strongest events, excluding extreme conditions like hurricanes, were typically associated with southeast winds as indicated by wind rose map (Fig. A2). Therefore, a 3-day southeast wind event with peak speeds reaching up to 8 m s^{-1} during days 127.5 – 130.5 in 2019 was used to investigate the bay wide stratification responses to this common summer wind forcing. This event was advantageous as the pre-event conditions had moderate discharge (~ 2, 000 m^3 s^{-1}, Fig. 2.1) and low wind conditions (~ 2 m s^{-1}, Fig. 3a) setting the stage for strong pre-event stratification in the system. The model performance was validated with long term monitoring data over the full year of the model run (Appendix A.1) as well as extensive field data collected 14 days prior to the studied wind event (Section 3.1; Fig. 2).

a. Model validation

Three quantitative indexes were applied to assess the model performance including mean error $ME = \frac{1}{N}\sum_{i=1}^{N}(M - O)$, mean absolute error $MAE = \frac{1}{N}\sum_{i=1}^{N}|M - O|$, and model skill $Skill = 1 - \frac{\sum_{i=1}^{N}|M-O|^2}{\sum_{i=1}^{N}(|M-\bar{O}|+|O-\bar{O}|)^2}$ (Wilmott 1981). Where O and M are the observed and modeled data, respectively. The overbar indicates the temporal average over the number of observations (*N*). The magnitudes of *ME* and *MAE* indicate the average bias and deviation between model and observation. *Skill* acts a global index of overall agreement between model and observation, where $Skill = 1$ denotes perfect agreement while $Skill = 0$ indicating complete disagreement.

Modeled time series of water level, salinity, and temperature at 0.5 m above bottom compared favorably with observed time series at multiple stations across the bay. Inside the bay, the modeled near-bottom salinity had a mean error of approximately 2 psu and the skill score was above 0.86 (Fig. A1, Table A1). The model captured the temperature patterns with a skill above 0.97. Additionally, the model captured both daily and seasonally hydrographic variations. Detailed model validation statistics are presented in Appendix A.1.

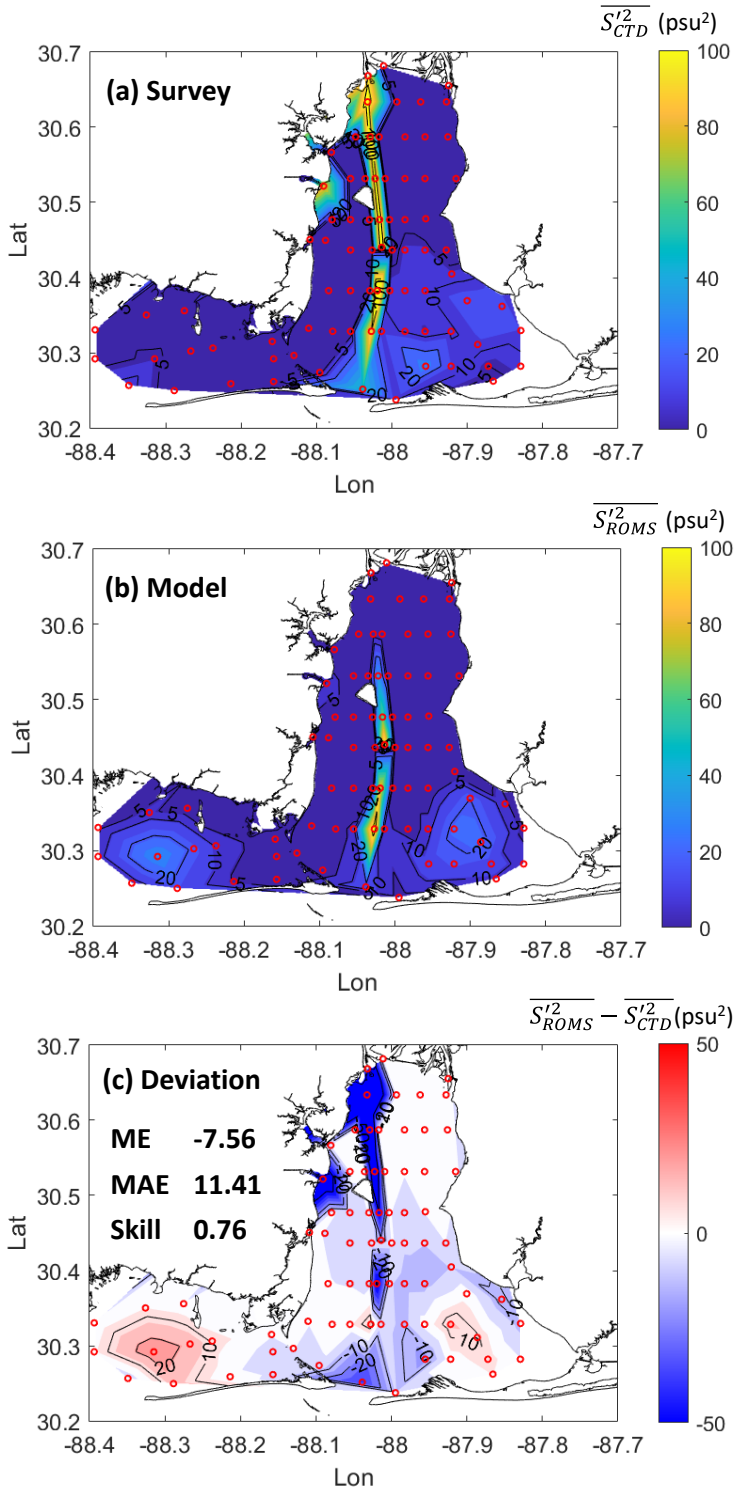

Fig. 2 Spatial patterns of depth averaged vertical salinity variance during days 112 - 113, 2019. (a) Data from CTD profiling, $\overline{S'^2_{CTD}}$. (b) Data from ROMS model outputs, $\overline{S'^2_{ROMS}}$. (c) Deviations between model results and CTD data, $\overline{S'^2_{ROMS}} - \overline{S'^2_{CTD}}$. Note that both $\overline{S'^2_{CTD}}$ and $\overline{S'^2_{ROMS}}$ were computed within water columns from 1m below surface to bottom. Red circles in the three panels denote CTD stations.

Besides observed time-series data, bay wide observed CTD profiles during days 112 – 113, 2019 (Coogan et al. 2021) allowed for the validation of the model capability to capture

stratification 14 days prior to the studied wind event. Overall, the model performed well with the mean errors between model outputs and survey data for near-surface, near-bottom, top-to-bottom salinity differences being -0.60 psu, -2.45 psu, and -1.85 psu respectively. The corresponding skill values were 0.95, 0.87 and 0.82 respectively, indicating that the model favorably captured salt dynamics inside the bay.

A final measure of model skill was obtained by comparing the depth averaged vertical salinity variance (Fig. 2). Qualitatively, Fig. 2b shows that the model spatially reproduced the observed salinity variance (Fig. 2a), where the strongest stratification (~ 100 psu^2) occurred in the shipping channel and moderate stratification (10 - 20 psu^2) occurred in the southeast and southwest regions (Fig. 2a, b). Quantitatively, a skill of 0.76 indicates stratification was well captured over the entire system (Fig. 2c). Locally, the model underestimated stratification at the northern end of the shipping channel and the channel connecting the ship channel to the Industrial canal. In both locations modeled bottom salinity was less than observed (Fig. 2b, c). The model also overestimated stratifications in parts of Mississippi Sound. These deviations led to a mean error of -7.56 psu^2. Note that our study area was focused on the mid- to lower bay, where deviations were within ±5 psu^2. Based on these skill statistics, the modeled stratification was deemed acceptable.

b. System response to southeast wind condition

The modeled vertical salinity variance and its relationship to stratification and wind forcing were analyzed for a wind event during days 127.5 – 130.5, 2019. Spatial variations in salinity variance and the calculated budget terms revealed the mechanisms controlling the spatial heterogeneity in the system response.

1) VERTICAL SALINITY VARIANCE

Strong pre-wind stratification was captured by the depth-average vertical salinity variance $\overline{S'^2}$ calculated from ROMS model hourly outputs (day 127.75, Fig. 3b). Just prior to the onset of the wind event (day 127.75, Fig. 3b), wind speed was only 1.86 m s^{-1}, the $\overline{S'^2}$ is above 15 psu^2 over most parts of the bay. Over the flanks of the bay, the 5 psu^2 isoline extended 36 km north of Main Pass. Peak $\overline{S'^2}$ of greater than 80 psu^2 occurred in the shipping channel and lower part of the bay near the mouth. Approximately 18 hours from the time when the wind transitioned to the southeasterly direction, wind speed increased to 4.71 m s^{-1}, but this had little effect on the spatial patterns of $\overline{S'^2}$ (Fig. 3c). Only the zone to the northeast of Main Pass

285 experienced a change with the $\overline{S'^2}$ decreasing from 75 - 80 psu^2 to 45 - 50 psu^2, a decline of
286 around 35 - 40 %. However, this was a relatively small area of the bay.

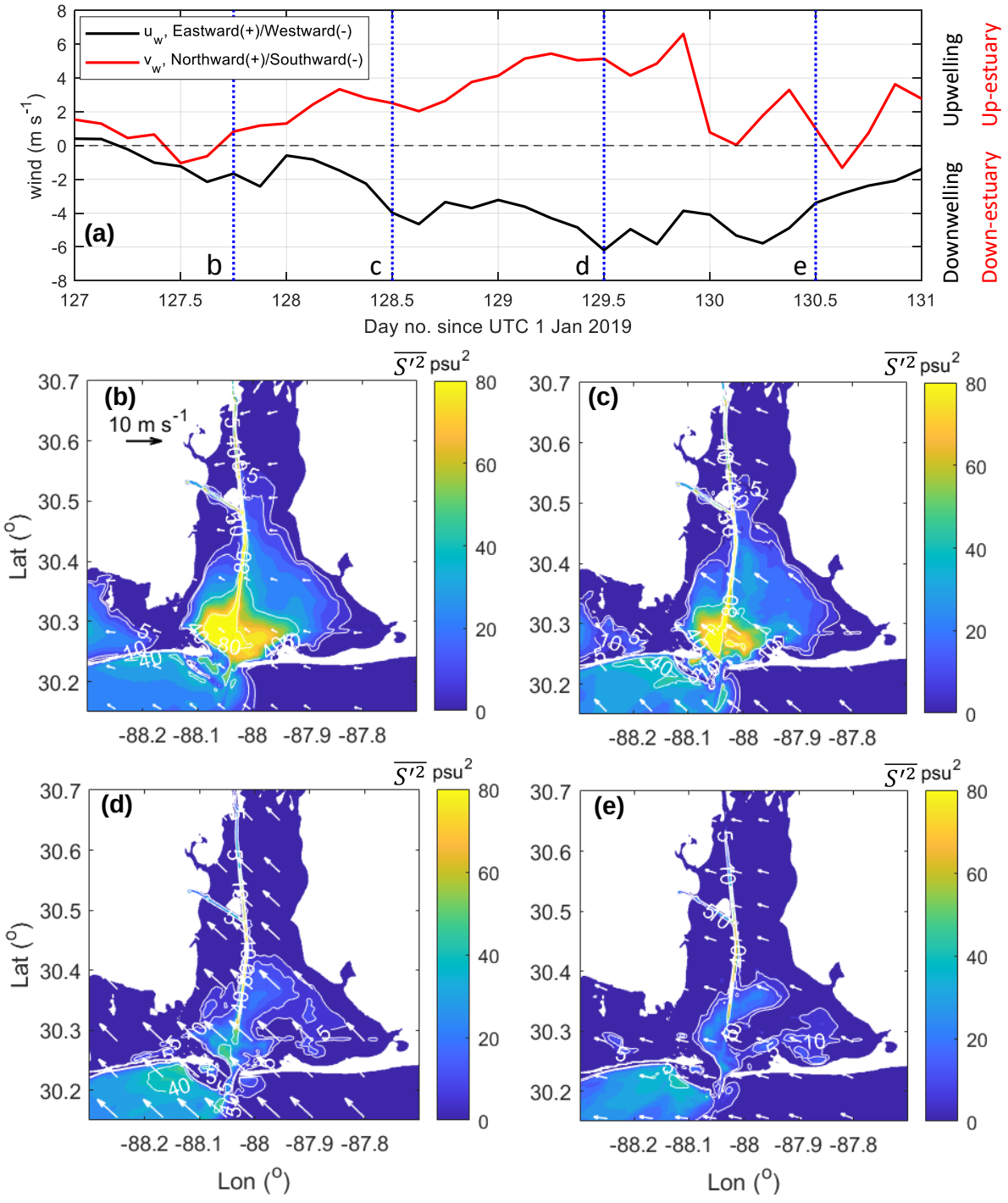

287

288 Fig. 3 Change in wind and evolution of mean water column vertical salinity variance, $\overline{S'^2}$, during a
289 southeast wind event on days 128-131, 2019. (a) 3-hour averaged raw wind speed in the center of Mobile
290 Bay from NARR, where blue dashed lines denote time ticks corresponding to different phases of the wind
291 event shown in panels b – e. Snapshots of the evolution of depth averaged salinity variance ($\overline{S'^2}$) over the
292 southeast wind event: (b) Event initiation, (c) Event onset, (d) Event peak, and (e) Event end. The spatial

structure of the wind is shown with white arrows and different level of $\overline{S'^2}$ are shown with solid white contours.

Noticeable impacts on stratification from the wind conditions were apparent at the peak wind speed of 8.05 m s^{-1} (day 129.5, Fig. 3d). Bay-wide decreases in stratification were observed with the $\overline{S'^2}$ being below 20 psu^2 in bay's entire eastern portion and many subsections in this area being under 10 psu^2. Stratification did remain in the shipping channel and lower western zone of the bay between the two tidal inlets, where the $\overline{S'^2}$ remained above 40 psu^2 (Fig. 3d). The highest $\overline{S'^2}$ with values above 80 psu^2 only occurred in the upper shipping channel away from the Main Pass. Additionally, the most north location of the 5 psu^2 isoline on the flank was 22 km north of Main Pass, a southward shift of 14 km when compared with pre-event state of the systems (Fig. 3b).

The peak wind speed lasted for 9 hours, at which point the atmospheric conditions transitioned to a period of relatively quiescent winds (Fig. 3a). This 9-hour peak wind duration further reduced bay wide stratification leaving only two weakly stratified belts in the lower half of the bay (Fig. 3e). One stratified region was orientated in the northeast-southwest direction perpendicular to wind direction and obliquely crossed the shipping channel. The other region followed the intracoastal water way to the east of the shipping channel near the south shore of the bay. While the southeast wind with a peak speed of 8 m s^{-1} was unable to completely mix the entire bay, the evolution of the $\overline{S'^2}$ highlights notable spatial heterogeneity of stratification and mixing in response to wind. To understand what caused the spatial heterogeneity and highlight wind influences on bay-wide stratification, the salinity variance budget is examined in the next section.

2) SALINITY VARIANCE BUDGET

Focusing on the core of the southeast wind event (days 128-130), the strength of the vertical salinity variance budget terms in Eq. (1) were used to identify the dominant processes contributing to the evolution of the bay-wide stratification (Fig. 4). As might be expected from the decrease in the $\overline{S'^2}$ over the course of the southeast wind event (Fig. 3), there was a negative tendency with magnitudes larger than 5 psu^2 d^{-1} (Fig. 4a). In the lower half of the bay, the tendency had higher intensities around 10 - 20 psu^2 d^{-1} indicating that southeast wind blowing over 1 day could completely mix weakly stratified zones (Fig. 4a). Maximum tendencies reached up to 50 psu^2 d^{-1} and occurred near Main Pass; however, the strongly stratified

conditions at those locations prior to the wind event ($\overline{S'^2}$ > 80 psu^2 in Fig. 3b) prevented this non-extreme wind event from completely mixing the water column. Curiously, positive tendencies above 4 psu^2 d^{-1} occurred at certain locations along the lower edge of the bay, the secondary inlet (Pass Aux Heron), and the south shore of Dauphin Island (Fig. 4a), indicating that southeast wind enhanced stratification in particular locations in the bay and compressed the Mobile Bay plume against the coast over the inner shelf. Regardless, the tendency term within the bay had a distinct spatial pattern in response to this non-extreme wind event.

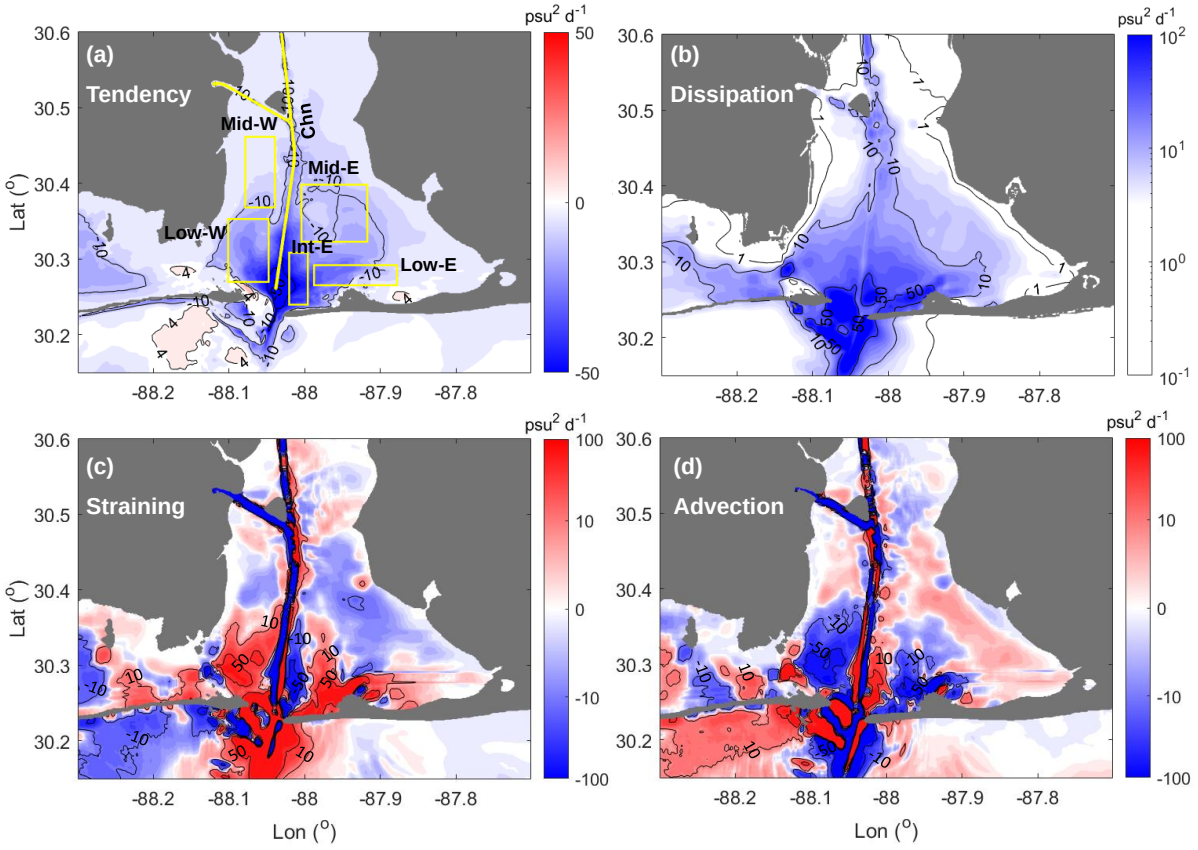

Fig. 4 Terms in the vertical salinity variance budget during a southeast wind event. All terms were temporally and vertically averaged from days 128 - 130 with the unit being psu^2/day. Red color denotes positive tendency, advection, and straining (i.e., stratifying processes); blue color denotes negative tendency, advection, straining and dissipation (i.e., de-stratifying processes). Yellow boxes with black labelling in panel (a) denotes averaging regions used to investigate the temporal evolution of the budget terms in Fig. 5.

The structuring of this spatial pattern was further explored by examining the contributions of the right-hand terms in Eq. (1). Qualitatively, there was a clear mirroring between the dissipation and tendency terms with dissipation > 10 psu^2 d^{-1} across most parts of the lower bay and the largest values (> 50 psu^2 d^{-1}) at the two tidal inlets (Fig. 4b). The straining and advection terms were also important with magnitudes greater than 10 psu^2 d^{-1} in some locations.

Positive straining, i.e., fresher water being advected over saltier water occurred in the lower bay away from the shipping channel (red color, Fig. 4c) where stratification remained. Whereas negative straining, i.e., saltier water being advected over fresher water, was concentrated next to the shipping channel near the mouth and in the mid-bay area (blue color, Fig. 4c) and acted to reduce stratification. Positive advection along the shipping channel near the mouth (red color, Fig. 4d) denoting the incoming transport of salinity variance to this region. In contrast, stratification was transported out of some regions as indicated by negative advection, e.g., zones away from the shipping channel in the lower bay (blue color, Fig. 4d). The southwest section of the bay highlights the complex nature of these processes contributing to the stratification patterns where the straining and advective terms exceed magnitudes of 50 $psu^2\ d^{-1}$, 3 - 4 times that of dissipation in this region. The contrasting signs with positive straining and negative advection limited the impact of these terms on the tendency term. Consequently, the mechanisms driving the general patterns in the salinity variance were notably heterogeneous.

Additional insight on the heterogeneity of the contributions to the tendency term can be seen in the time evolution of the budget terms in different regions of the bay. Six regions including the shipping channel and those to east and west of the shipping channel were selected to highlight changes with distance from the mouth of the system as well as west-east asymmetries. At the mid-bay regions (Mid-W and Mid-E), negative straining together with wind induced variance dissipation resulted in well mixed (Fig. 5a) or weakly stratified conditions (Fig. 5b). In the lower part of the bay (Low-W and Low-E), there was a shift in the contributions of terms in the variance budget, where increases in straining and advection reduced the impact of dissipation (Fig. 5c, d). This shift away from the importance of dissipation can also be seen throughout the length of the shipping channel where stratification presented a neglectable tendency over the course of the event from an imbalance between positive staining and negative advection rather than dissipation (Fig. 5f).

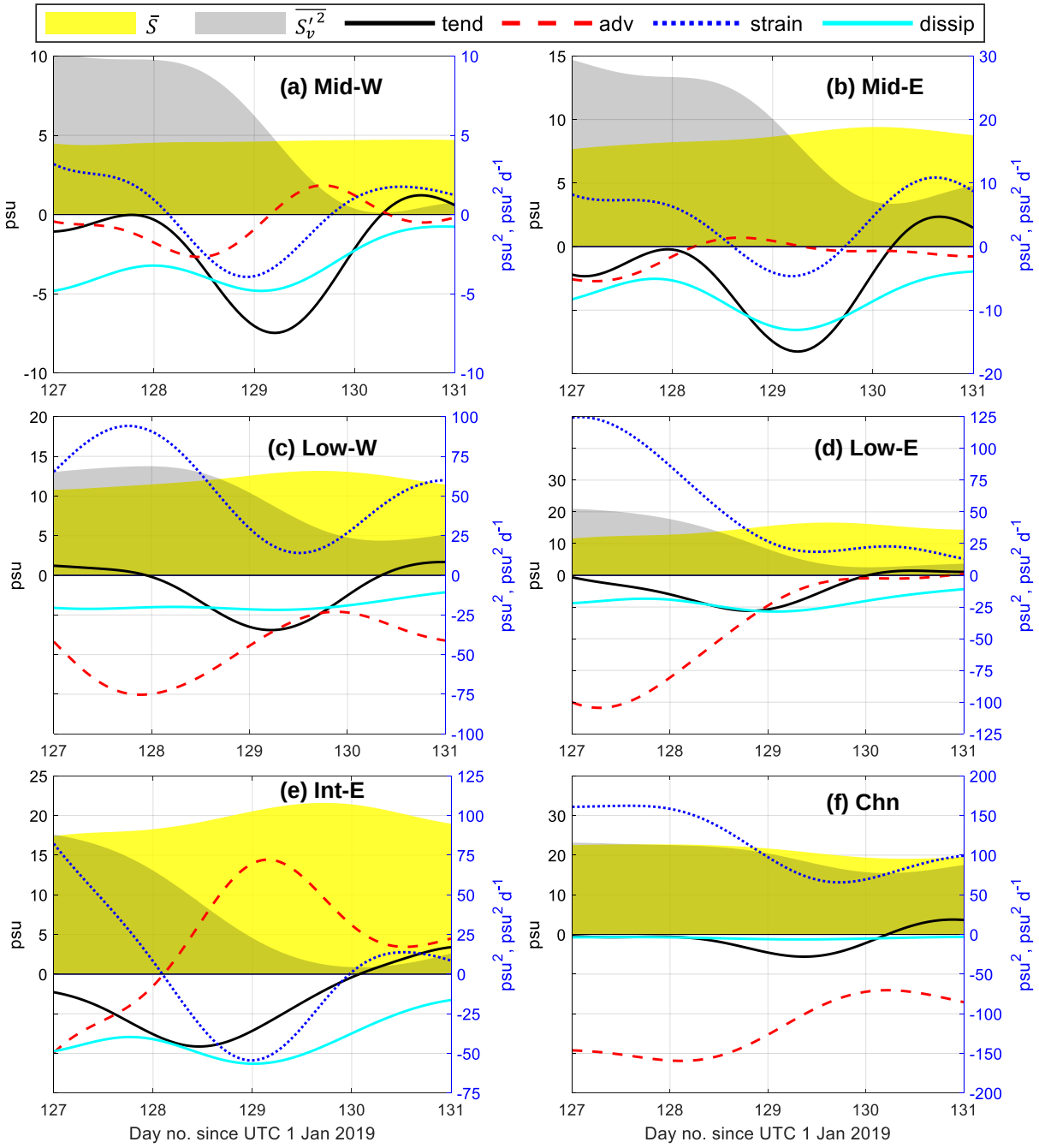

Fig. 5 Time series of the low pass filtered spatially averaged salinity $\bar{S}$, salinity variance $\overline{S'^2}$ and budget terms during a southeast wind event from days 128 - 130 for several regions of the bay. The averaging regions in the panels are denoted by the corresponding yellow boxes in Fig. 4a.

On the east and west flanks positive straining was able to marginally overcome advection and dissipation which allowed this region to remain weakly stratified (Fig. 3e). Near the tidal inlet (Int-E), positive advection denoted incoming transport of salinity variance which was overwhelmed by dissipation and negative straining leading to a region of well mixed waters (Fig. 5e). This input of salinity variance by advection near the mouth (i.e., the transport of salty

Gulf of Mexico water) is consistent with the general increase in the subtidal volume averaged salinity across the bay during this southeast wind event (Fig. 5a ~ 5e). The impact of this salty water from the Gulf is more complex once it entered the bay as can be seen for the temporally and spatially varying contributions of the advective term in the salinity variance budget.

Consequently, the spatial heterogeneity in mixing of the bay in response to this southeast wind event was caused by the deviations in the relative strength among advection, straining and dissipation. In the middle bay away from the tidal inlet, negative straining together with vertical mixing weakens stratification. Moving to the lower bay, straining changes signs across the estuary and advective contributions were intensified. Since both straining and advection link to the circulation and salt transport, further discussion of the wind influence on circulation and salt transport is required.

c. Wind induced circulation and transport

During the wind event, the circulation did not follow typical estuarine exchange flow where the horizontal density gradient drives surface outflow and bottom inflow. The estuary was clearly responding to both local and remote wind-forcing. The impacts of local stress were apparent with the southeast wind driving surface currents generally up-estuary in the direction of the wind (Fig. 6a) while the bottom current generally flowed down-estuary (Fig. 6b), opposite that of typical estuarine subtidal flow patterns. The morphology of the bay appeared to modify the local response to wind forcing to some extent. For example, the width of the lower bay allowed much of the return circulation along the bottom towards the southeast and nearly opposite the wind direction from the southeast, rather than being directed toward the systems exits of Main Pass and Pass Aux Herons. In addition, there was a recirculation feature in the surface currents in the northeast corner of the bay across from the mid-bay island and a region of bottom flow stagnation in the southwest corner of the bay associated with flow constraint from Pass Aux Herons. These patterns highlight important deviations from the idealized scenarios of wind forcing in simplified estuarine geometries. Notably, these modifications to the local wind response have a significant impact on the stratification and mixing across the system. For example, the significant spatial differences in the bottom currents, where intensified down-estuary current (around 0.1 m s^{-1}) only existed over the southeastern portion of the bay compared to the less than 0.05 m s^{-1} in the southwestern part (Fig. 6b), agreed well with intensified mixing in southeast region (Low-E, Fig. 5d) relative to that in the southwest region of the bay (Low-W, Fig. 5c). The asymmetric responses across the

estuary were also reported in Chesapeake Bay under typical summer wind conditions (Scully 2010a), where significant portions of the cross section remain stratified while certain regions frequently experience mixing.

The direct impacts of the remote wind forcing are concentrated at the mouth of the system (i.e., Main Pass) where the along-shelf component of the wind driven net Ekman transport was onshore at the coast. This enhanced subtidal inflow (0.05 - 0.1 cm s^{-1}) throughout the deep shipping channel and weakened outflows over the shoals (Fig. 7). Importantly, the incoming shelf waters encountered southeastward bottom currents driven by the local wind stress just behind the tidal inlet corresponding to the location of an intensified mixing zone (Fig. 4b, 5e) and re-directed the shelf inflow eastward bringing salty waters and the associated salinity variance into the east part of lower bay (Low-E, Fig. 5d).

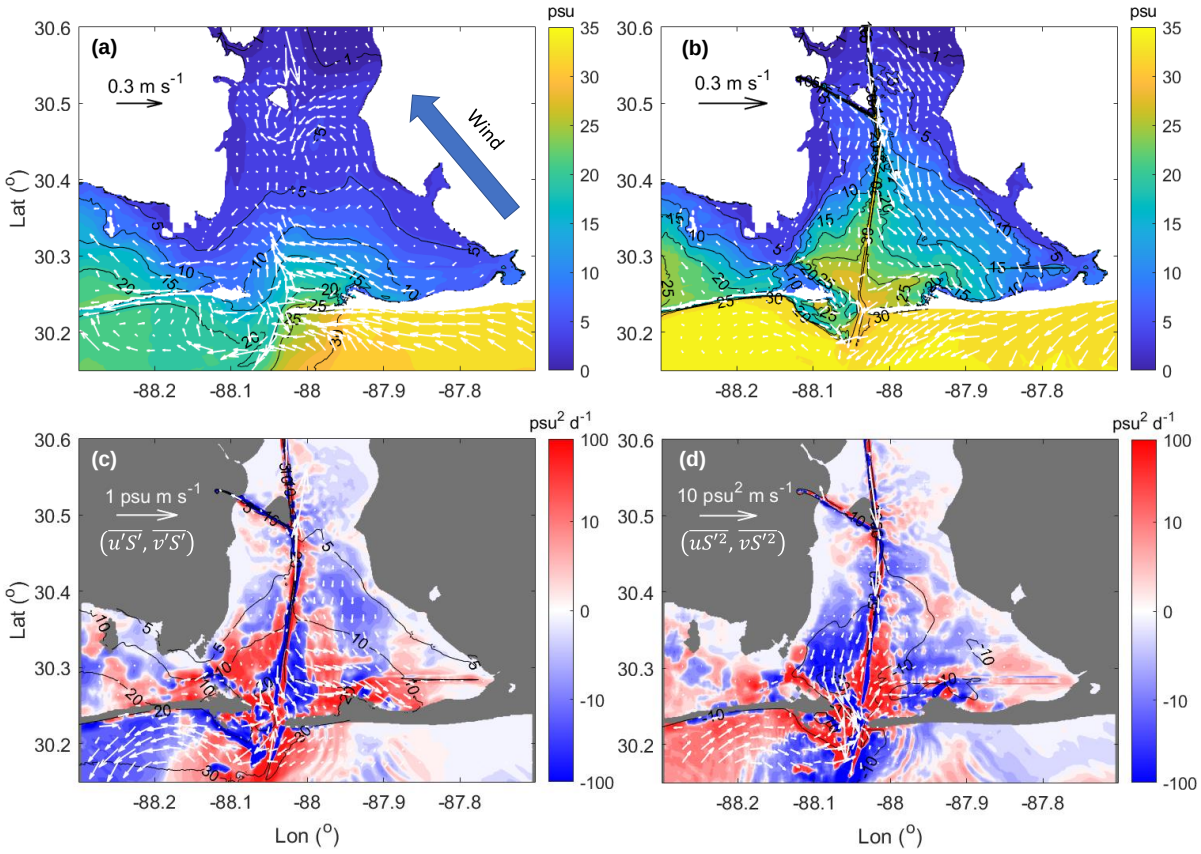

Fig. 6 Low pass filtered current (vectors) and salinity (contour lines) during peak southeast wind speed (day 129.5) at surface (a) and bottom (b). (c) Low pass filtered depth averaged salt flux (vectors), salinity (contour lines), and straining terms in the salinity variance budget (coloration). (d) Low pass filtered depth averaged salinity variance flux $\overline{uS'^2}$ and $\overline{vS'^2}$ (vectors), salinity variance (contour lines), and advection term in salinity variance budget (coloration). Red denotes convergence (incoming) of salinity variance flux, blue color divergence (outgoing) of salinity variance flux.

d. Impact of the circulation on the salt flux and salinity variance

As the wind forcing interacts with underlying horizontal salinity gradients and associated gravitational flow, straining terms in the salinity variance budget broader range of impacts throughout lower Mobile Bay and at system inlets Main Pass and Pass Aux Herons. In the east portion of the bay (Fig. 6a, b), the reversal of the subtidal currents leads to a down-estuary salt flux and negative straining (Fig. 4c and Fig. 6c, blue color). While on the western flank there was positive staining. This was due, in part, to fresher water being forced westward as shown by the asymmetry in salinity gradients across the system, i.e., much stronger salinity gradients in the to the west (Fig. 6c). But, also due to weak bottom currents coupled with the westward component of the surface currents (Fig. 6a) which transported this pool of relatively fresher water over the salty water entering from eastern Mississippi sound. As such, there was salt flux into Mobile Bay and positive straining in this region (Fig. 4c and Fig. 6c, red color). Additional regions of positive straining were observed in the southeast section of the bay just beyond Main Pass. Here, eastward current at bottom transported salt into the fresher area of the lower part of the bay resulting in positive staining (red color in the lower east part of Fig. 6c). Consequently, the salinity associated with the incoming shelf waters tended to stratify the water column and competed with wind induced mixing, particularly in the lower eastern part of the bay (Low-E, Fig. 5d). These patterns in the straining term were directly linked to the changes in the system circulation and salinity patterns induced by the wind-forcing.

Additional impacts of wind forcing on the salinity variance budget were derived from the advection of stratification via the regions of convergence or divergence throughout the bay. The dominance of this term, as mentioned in section 3.2.2, was focused on the lower bay especially around Main Pass (Low-W, Fig. 5c and Int-E, Fig. 5e). To further understand the patterns in the advective component, the low pass filtered depth average salinity variance flux was further examined (Fig. 6d). Noticeably, in the southwestern region of the bay (Low-W), a distinct down-estuary salinity variance flux reached up to 10 psu^2 m s^{-1} and moved out of the system through the west portion of the tidal inlet. Therefore, the outgoing advection of salinity variance together with mixing via dissipation reduced stratification in the lower southwestern portion of the bay (Low-W, Fig. 5c). In addition, in the lower portion of the mid-bay, the incoming northward flowing shelf water and westward surface current from the eastern bay (Fig. 6a) generated a convergent zone of salinity variance, i.e., positive advective contribution to the salinity variance tendency (Fig. 6d and Fig. 5d). However, the convergence of salinity variance did not enhance the stratification because it was eliminated by negative staining and mixing.

The incoming flow and salt transport through Main Pass dominates the stratification responses in the lower bay due to bay-shelf connectivity during southeast wind conditions. This can be readily seen by comparing the structure of the flow across Main Pass during the pre-event and peak event periods. Under low wind speed before the southeast wind event, subtidal inflows at the tidal inlet had inflow (0.05 - 0.09 m s^{-1}) only in the deep channel, while outflow (0.1 - 0.45 m s^{-1}) was through the shoals and at the surface over the deep channel with a net outgoing flux of 1,515 m^3 s^{-1} (Fig. 7a). At peak wind speed, the net outgoing flux was reduced to 133 m^3 s^{-1}, where inflow was through the entire water column in the channel with maximum magnitudes of up to 0.13 m s^{-1} (Fig. 7c). Outflow current speeds were below 0.1 m s^{-1}, which equated to a reduction of almost half that during the low wind conditions prior to the event.

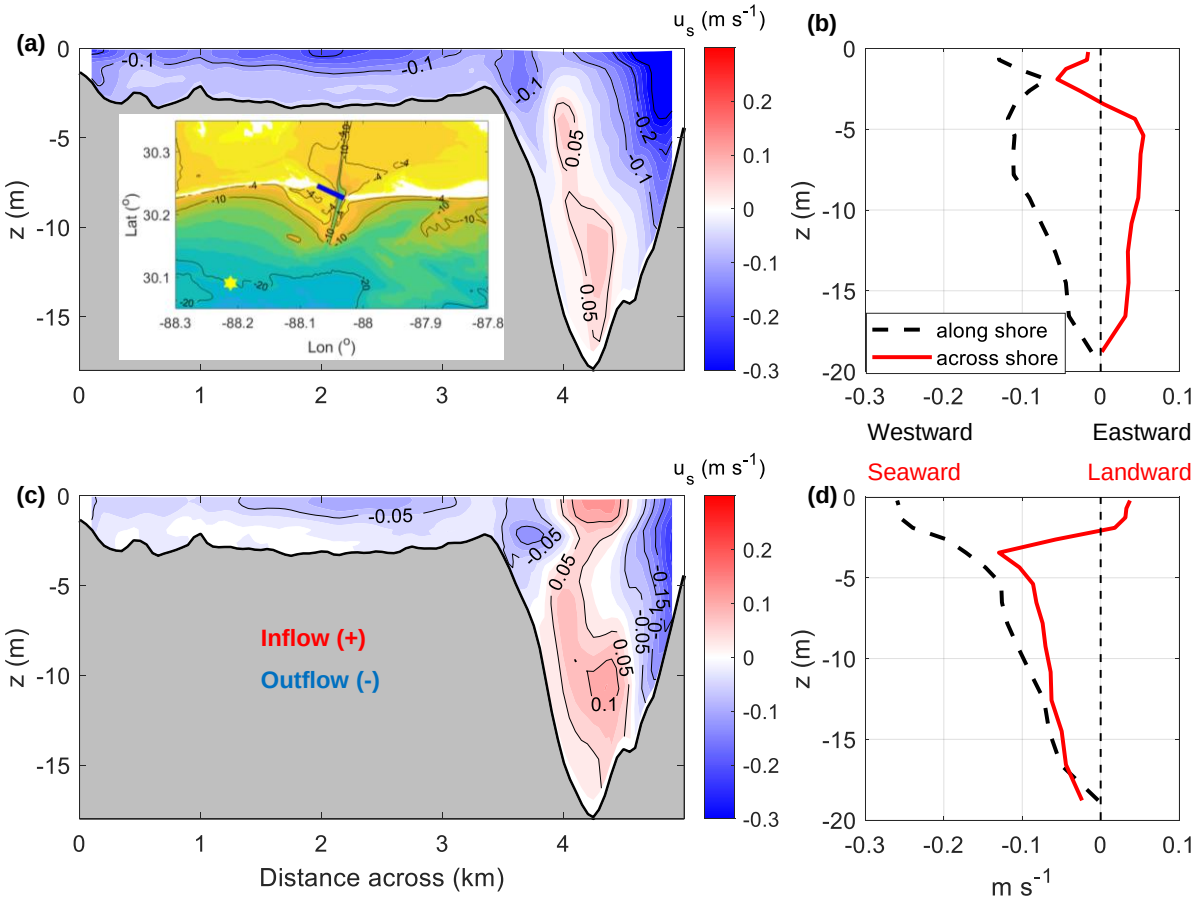

Fig. 7 Low pass flow patterns at Main Pass (a, b) and offshore (c, d) without significant wind on day 127.5 (a - b) and peak southeast wind on day 129.5 (c - d). In (a) and (c), red color denotes inflow (+) to the bay and blue color denotes outflow (-) from the bay. Subpanel of (a) shows where the transect across the tidal inlet (blue solid line) is located as well as the location of the offshore velocity point (yellow star). Coloration and black contour lines denote bathymetry in meters.

This enhanced inflow at Main Pass is consistent with expectations during downwelling wind events as indicated by the shelf currents. Broader shelf (Fig. 6a, b) as well as velocities from a representative site offshore (Fig. 7d) had westward along-shore currents and an across-

shore structure with landward surface currents and seaward subsurface current. Consequently, the estuarine-shelf connectivity through the advection of salinity variance from the shelf via coastal Ekman dynamics, in this case a downwelling event, had a notable impact on stratification and mixing patterns inside of the bay.

4. Discussion and Conclusions

Using a high-resolution regional scale model, a comprehensive study of realistic wind influences on stratification on a wide, shallow, microtidal estuary was conducted. Analysis of vertical salinity variance and the spatial-temporal variability in the local budgets revealed complexities of wind effects in such estuarine systems. This work highlights that the straining can be modified or inhibited by the wind and leads to complex interactions and the spatial variability observed in Fig. 3. The southeast wind with speeds up to 8 m s^{-1} acting at an angle to the along-axis direction of the system was effective at reducing bay-wide stratification through both weakening or reversing horizontal density straining and through direct wind mixing. There was significant spatial heterogeneity in the water column response where some regions were well mixed while others remained stratified after the wind event. This spatial heterogeneity in the stratification responses resulted from spatial variability in dominant physical processes, which in turn lead to spatially varying salinity variance budgets.

These differences in the local salinity variance budgets were linked to the relative impacts of different responses to wind forcing (i.e., direct mixing, wind straining, and remote effects, Fig. 8). In this typical wind event, the southeast wind reduced bay-wide stratification not only by local wind stress but also through remote wind induced Ekman transport of shelf waters. In the mid-bay away from the tidal inlets, the nature of the bay allows the non-axial wind forcing to generate a subtidal current pattern counter to the typical gravitational circulation that cleared the stratification from this region by causing both negative straining and direct mixing. In the southeast region, intensified down-estuary bottom current further enhanced mixing. In contrast, the lower western bay experienced a lateral transport of freshwater which caused positive straining that was balanced by advection of salinity variance out of the system through western shallows of Main Pass. The incoming shelf current through the ship deep channel from the coastal downwelling (i.e., remote wind forcing) brought salt into the system generating positive straining over the lower eastern bay and negative straining in the lower mid-bay region just north of Main Pass, resulting in these areas experiencing differing rates of mixing over the course of the event. Importantly, both the wind induced estuarine circulation as well as Ekman

transport from the shelf contributed to the spatial heterogeneity stratification in the bay. This work highlights that straining and direct turbulent mixing from surface wind stress dominated the stratification responses away from the inlets. Uniform stratification responses to winds are not expected in wide systems since bathymetry and coastline orientation promote heterogeneities in realistic systems. As Mobile Bay is representative of other estuaries in the northern Gulf of Mexico and other coastal region in the world, the complex interaction of dissipation, straining and advection in response to wind events need to be considered to fully understanding the stratification dynamics in these types of systems.

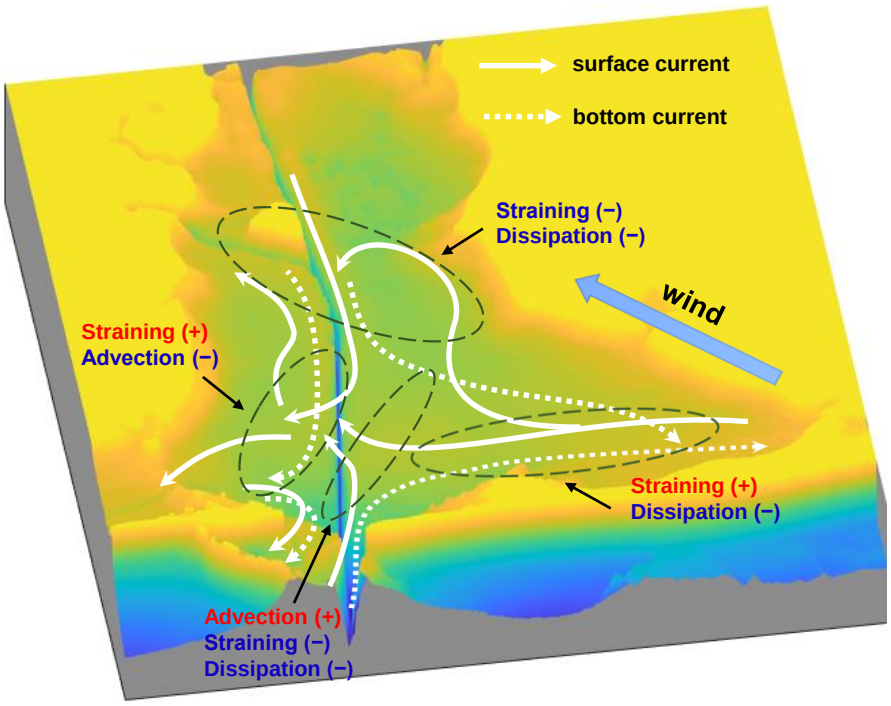

Fig. 8 Schematic diagram of flow patterns and stratification responses to southeast wind in Mobile Bay. The solid (dashed) white arrows indicate surface (bottom) flow, and the grey dashed circles indicates zone where different process are modifying the stratification.

While this case study focuses on one event that commonly occurs in the summer, there are other aspects of wind forcing that should be explored in future work. Consideration of wind forcing from other common directions such as southwest wind in the summer season or cold front events in the fall-winter-spring would help inform system response to wind forcing by comprehensively mapping the complex balance between the transport, straining, and dissipation terms. In fact, Scully (2010b), demonstrated that changes in the wind direction had impacts on the mixing dynamics of Chesapeake Bay which led to significant differences in the

level of summer-time hypoxia. The relative importance of wind direction in modifying the mixing dynamics in shallow, wide systems like Mobile Bay remains an open question.

The effect of waves can modify the effectiveness of wind stress in transferring momentum into the water, potentially enhancing mixing through breaking and increasing turbulence at surface as well as wave-current interactions. As we did not include these wave effects, the findings of this work may be a conservative estimate of the mixing expected during non-extreme wind events. Further studies on quantifying wind-driven wave influences in stratification responses would further improve the understanding of wind-induced mixing especially in wide, shallow, and stratified estuaries like Mobile Bay (Chen et al. 2005a, 2005b).

Acknowledgments.

This project was funded by NOAA RESTORE Program "Building Resilience for Oysters, Blue Crabs, and Spotted Seatrout to Environmental Trends and Variability in the Gulf of Mexico" (NOAA RESTORE NA19NOS4510194). This work used the Extreme Science and Engineering Discovery Environment (XSEDE), which is supported by National Science Foundation grant number ACI-1548562; service was provided by Expanse at San Diego Supercomputer Center (SDSC) through allocation EES210015. This work would not have been possible without the many folks that have passed through the Tech Support Group at the Dauphin Island Sea Lab to help maintain the Alabama Real-time Coastal Observing System over the years. We would like to sincerely thank Dr. David Ralston for helping build up the numerical model using ROMS. We also would like to thank Dr. Steve Dykstra for sharing the latest bathymetry data in Mobile River, Tombigbee River, and the shipping channel.

Data Availability Statement.

All the field data used for model validation is accessible through the link https://arcos.disl.org/. All data that were not downloaded from public sources have been made publicly available through the Dauphin Island Data Management Center (https://www.disl.edu/research/data-management-center) and (or have been submitted to) the

NOAA National Center for Environmental Information (NCEI). Site CP data are available at the following links:

https://accession.nodc.noaa.gov/0211052

https://www.ncei.noaa.gov/access/metadata/landing-page/bin/iso?id=gov.noaa.nodc:0241013

https://data.nodc.noaa.gov/cgi-bin/iso?id=gov.noaa.nodc:0203749.

APPENDIX

Appendix A Hydrographic validation in 2019

In 2019 the river discharge generally varied between 1,000 m^3 s^{-1} and 9,900 m^3 s^{-1} in the early wet season (day no. 1 - 143) and reached a maximum value of 9,911 m^3 s^{-1} (Fig. A1b.1). In the dry season (day no. 144 - 298) river discharge was only 200 – 1,000 m^3 s^{-1}. The seasonal and sub-seasonal variability follows regular patterns reported in previous studies (Kim and Park 2012). Model performance was validated by comparing hourly and 48-hour low-pass filtered subtidal hydrodynamic and hydrographic outputs with field observations.

A.1 Water level

The model results of water level were compared with observation data at NOAA tide station 8735523 at Fowl River (FR, Fig. A1a). The model captured the diurnal tidal elevation with a *Skill* = 0.91 for total water level yet underestimated mean water level by 0.03 m (Table A1). The averaged deviation of total water level was 0.085m while the subtidal water level deviation was up to 0.07 m, indicating that most of the errors rise from subtidal water level. These errors in the subtidal water level likely result from effects associated with the wind forcing and the imposed non-tidal water level and current at open boundaries.

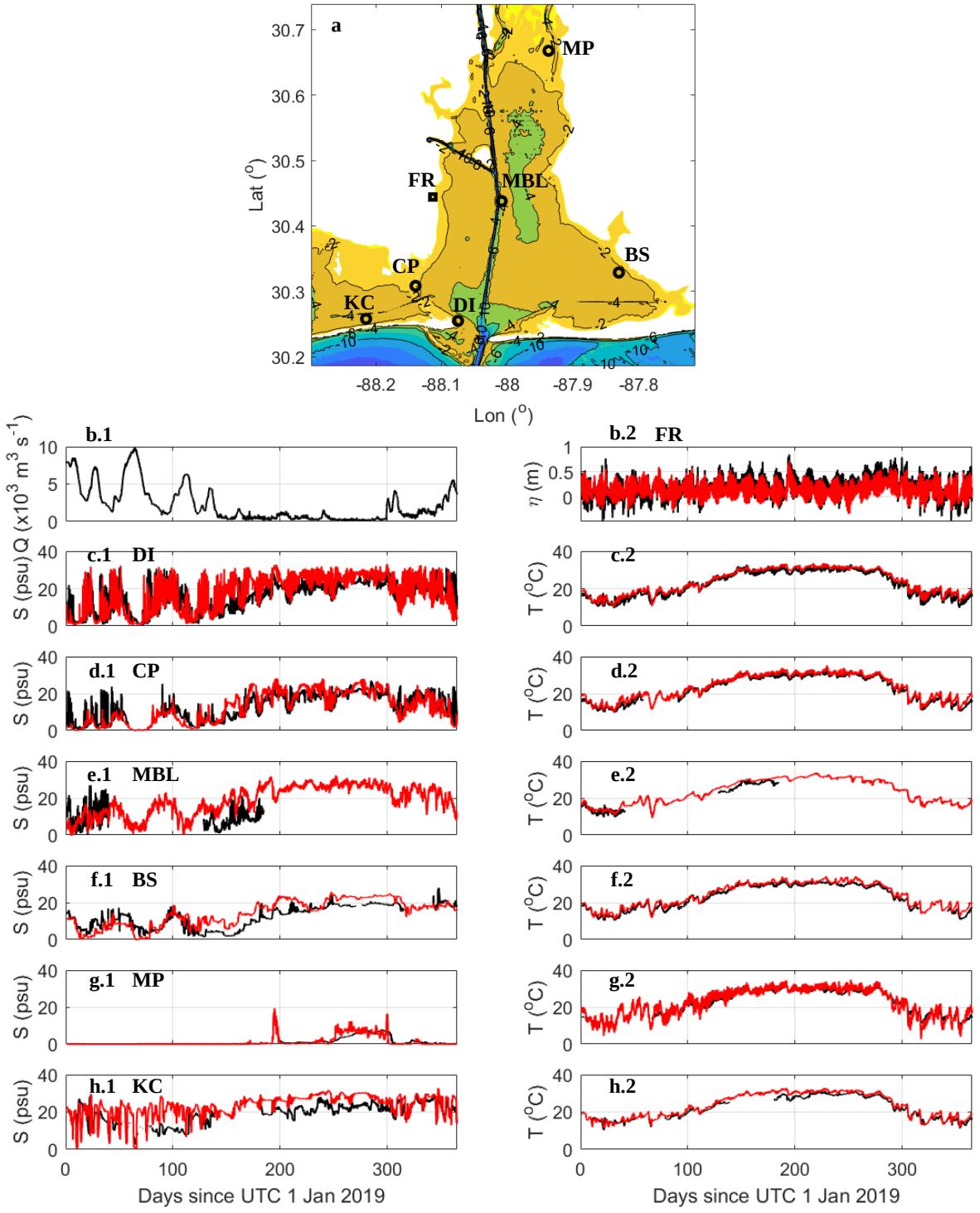

Fig. A1 Data to model comparison of the hydrodynamic and hydrograph variables in year 2019. (a) Map of observation stations at Fowl River (FR), Dauphin Island (DI), Katrina Cut (KC), Bon Secour (BS), and Meaher Park (MP). The water level station at Fowl River is NOAA tide station 8735523. Other stations are hydrographic stations deployed by ARCOS. (b.1) River discharge in 2019 with the data being the summed discharge at USGS stations 02428400, 02469761, and 02469800. (b.2) Water level from at a NOAA tide station in the central bay region. (c - h) Salinity and temperature at 0.5 m above bottom from ARCOS stations. In all plots the data is represented as black lines and model output by red lines.

599 Table A1 Error estimates for model-data comparison for 2019.

Variables	Station	Total			Subtidal	
		ME	MAE	Skill	MAE	Skill
Water level (m)	Fowl River (FR)	-0.031	0.087	0.91	0.070	0.85
Salinity (PSU)	Dauphin Island (DI)	2.13	4.76	0.86	4.00	0.90
	Cedar Point (CP)	0.30	3.35	0.90	3.05	0.93
	Middle Bay Light (MBL)	5.13 (2.36) *	8.09 (6.51)	0.43 (0.48)	7.63 (6.13)	0.43 (0.49)
	Bon Secour (BS)	1.94	4.01	0.87	3.94	0.87
	Meaher Park (MP)	0.06	0.73	0.89	0.71	0.90
	Katrina Cut (KC)	4.60	5.67	0.69	5.43	0.69
Temperature (^{o}C)	Dauphin Island (DI)	1.35	1.48	0.98	1.39	0.99
	Cedar Point (CP)	1.22	1.33	0.99	1.28	0.99
	Middle Bay Light (MBL)	1.62 (1.15)	1.76 (1.79)	0.98 (0.98)	1.69 (1.74)	0.98 (0.98)
	Bon Secour (BS)	1.41	1.49	0.97	1.47	0.98
	Meaher Park (MP)	0.37	1.67	0.97	1.48	0.98
	Katrina Cut (KC)	1.25	1.46	0.98	1.49	0.98

600 * Denotes model results at 1 m above bottom at Middle Bay Light station.

601 ## A.2 Salinity

602 The salinity at 0.5 m above the bottom ($S_{b0.5}$) was compared with field data from Alabama's
603 Real-Time Coastal Observation System (ARCOS). At most stations, the mean bias and
604 deviation of salinity results was around 2 psu and 4 psu, respectively, for the total and subtidal
605 components. The skill ranged from 0.86 - 0.90 for total salinity and 0.87 - 0.93 for the subtidal
606 component (Table A1). The model captured the predominant tidal driven daily cycle of
607 exchange between the fresher bay and the salty Gulf of Mexico at Dauphin Island station near
608 Main Pass (Fig. A1c.1). In the wet season (days 1- 150), when river discharge was between
609 1,000 – 5,000 m^3 s^{-1}, the near-bottom salinity $S_{b0.5}$ varied more than 25 psu within one diurnal
610 tidal cycle indicative of the advective transport occurring at the mouth. When river discharge
611 was above 7, 000 m^3 s^{-1} (days 60 - 70), fresh water flushed salt out of the system leaving the
612 bay totally fresh, where $S_{b0.5}$ at the Dauphin Island station dropped to zero (Fig. A1c.1). The

transition to the dry season (days 150 - 300) with a temporal mean of 19.5 psu took almost 50 days for $S_{b0.5}$ at Dauphin Island station. The dry season experienced a notable reduction in a tidal component with a diurnal cycle of ~ 10 psu. Similar pattern occurred at Cedar Point station near Pass Aux Herons (Fig. A1d.1), but the variation magnitude was almost half of that at Dauphin Island station. Thus, the temporally averaged salinity and tidal variance near the tidal inlets were sensitive to river discharge.

Tidal variation was also observed right next to the shipping channel in mid-bay at Middle Bay Light station (Fig. A1e.1). $S_{b0.5}$ varied between 10 psu to 25 psu in the wet season (days 1 - 40) denoting that salty water spilled out of the shipping channel to the flank via lateral advection during flood tide. Due the sharp bathymetry associated with the transition from the deep ship channel (~ 10 - 12 m) to the flat shoals (~ 3 - 4 m), high vertical and horizontal salinity gradients were expected at in region near this interface. This was confirmed as the mean bias dropped below 3 psu and model skill increased to 0.48 by sampling moving model comparison point upward by 0.5 m (Table A1). Usually, the sharp gradient in bathymetry challenges performance of sigma-coordinate based model. Despite notably weaker skill score at this location, the CTD survey in April (Fig. 2), indicate that the dynamics in the ship channel are being reasonably represented.

Salinity pattern presented less tidal variation moving into the bay. At Bon Secour station, $S_{b0.5}$ demonstrated only seasonal variability. In the wet season, $S_{b0.5}$ oscillated between 2 and 18 psu and was negatively correlated to the river discharge (Fig. A1f.1). In the dry season, this station increased from 2 to 15 psu through days 150 - 200. When the mean river discharge minimized to 330 $m^3 s^{-1}$ (days 200 - 300), $S_{b0.5}$ maintained a salinity ~ 20 psu with imperceptible tidal variation. Moving further to Meaher Park station, $S_{b0.5}$ was below 1 psu during most time of the year, but it reached up to 8 psu in days 280 – 300 and then rapidly dropped to zero when the next wet season arrived in October (Fig. A1g.1). Consequently, the model was able to capture seasonal salt penetration through the entire bay by late dry season as well as the seasonal impact of the river discharge episodically flush of the salt from the system.

In eastern Mississippi Sound outside of Pass Aux Heron, $S_{b0.5}$ presented little tidal variation but was much more sensitive to the water level in the wet season. At Katrina Cut station, $S_{b0.5}$ displayed notable perturbations with a period close to 10 days in early wet season synchronous to water level descent. For example, $S_{b0.5}$ experienced a sharp drop from 20 psu to 8 psu in

conjunction with a water level set-down of more than 1.1 m around day 20 (Fig. A1b.2, 2h.1). In the dry season, $S_{b0.5}$ at Katrina Cut station was mostly above 20 psu with weak fluctuations.

Both the model and observation captured the river discharge dominated seasonal and intra-seasonal variability in both Mobile Bay and nearby Mississippi Sound. Over the course of a year, near-bottom salinity demonstrated obvious sensitivity to both discharge and water level in wet season, while remaining stationary in the dry season due to low discharge. On a daily timescale, tidal driven variation was largest at the inlets and shipping channel and weakened rapidly away from those regions. The model well reproduces the salinity at the inlets suggesting good performance in simulating both bay-wide and shelf-wide transport.

A.3 Temperature

The model demonstrates excellent performance in simulating water temperature. The temperature at 0.5 m above bottom ($T_{b0.5}$) was compared with field data from ARCOS. Globally, the model overestimated $T_{b0.5}$ by around 1.4 ^{o}C with model skill values above 0.97 (Table A1). For this shallow system, the model performance in simulating thermal dynamics relies on external forcing to a great extent; the net solar radiation and air-sea heat exchange dominates water temperature.

The temperature only demonstrated temporal variability. In 2019, the annually averaged $T_{b0.5}$ was 22 – 23 ^{o}C. The maximum $T_{b0.5}$ was around 33 ^{o}C, while minimum value was 9.5 – 10.3 ^{o}C (Fig. A1c.2 – h.2). In summer (days 150 - 250), the water was stable with an averaged value of $T_{b0.5}$ around 29.1 – 29.9 ^{o}C. In winter and early spring, a cold front could cause short term temperature drops of 5 ^{o}C within several days. For example, during days 62 – 66, $T_{b0.5}$ dropped by 7 – 8 ^{o}C all over the bay within 3 days (Fig. A1c.2, 2d.2). The tidal signal in $T_{b0.5}$ was only observed at Dauphin Island station. For example, during days 29 - 35 after a peak river discharge of 7, 100 m^3 s^{-1}, $T_{b0.5}$ showed a tidal variation of 6.5 ^{o}C, indicating that tide driven flow exchange between the bay and the gulf at the inlet could alter local hydrography tremendously under certain river runoff conditions.

The model skill values were mostly above 0.86 for water level, near-bottom salinity, and temperature inside Mobile Bay, and the model captured multiscale processes including seasonal, intra-seasonal and tidal variability in both salt and thermal dynamics. Considering the complexity of this system with multiple inlets, an extensive river-delt-bay transition, and

674 channel-shoal bathymetry, we believe the model captured the physical processes in Mobile Bay
675 exceptionally well.

676

677

678 REFERENCES

679 ADCIRC, 2001: Western North Atlantic, Caribbean and Gulf of Mexico Tidal Databases.
680 Latest accessed 3 June 2022, https://adcirc.org/products/adcirc-tidal-databases/

681 Amante, C., Love, M.R., Taylor, L.A. and Eakins, B.W., 2011. Digital elevation models of
682 Mobile, Alabama: procedures, data sources, and analysis.

683 Barnier, B., Siefridt, L. and Marchesiello, P., 1995. Thermal forcing for a global ocean
684 circulation model using a three-year climatology of ECMWF analyses. *Journal of Marine*
685 *Systems*, 6(4), pp.363-380.

686 Burchard, H., 2009. Combined effects of wind, tide, and horizontal density gradients on
687 stratification in estuaries and coastal seas. *Journal of Physical Oceanography*, 39(9),
688 pp.2117-2136.

689 Burchard, H. and Rennau, H., 2008. Comparative quantification of physically and
690 numerically induced mixing in ocean models. *Ocean Modelling*, 20(3), pp.293-311.

691 Burchard, H., Hetland, R.D., Schulz, E. and Schuttelaars, H.M., 2011. Drivers of residual
692 estuarine circulation in tidally energetic estuaries: Straight and irrotational channels with
693 parabolic cross section. *Journal of Physical Oceanography*, 41(3), pp.548-570.
694 https://doi.org/10.1175/2010JPO4453.1.

695 Burchard, H., Janssen, F., Bolding, K., Umlauf, L. and Rennau, H., 2009. Model simulations
696 of dense bottom currents in the Western Baltic Sea. *Continental Shelf Research*, 29(1),
697 pp.205-220.

698 Bye, J.A., 1988. The coupling of wave drift and wind velocity profiles. *Journal of Marine*
699 *Research*, 46(3), pp.457-472.

700 Cambazoglu, M.K., Soto, I.M., Howden, S.D., Dzwonkowski, B., Fitzpatrick, P.J., Arnone,
701 R.A., Jacobs, G.A. and Lau, Y.H., 2017. Inflow of shelf waters into the Mississippi
702 Sound and Mobile Bay estuaries in October 2015. *Journal of Applied Remote*
703 *Sensing*, 11(3), p.032410.

Chant, R.J., Geyer, W.R., Houghton, R., Hunter, E. and Lerczak, J., 2007. Estuarine boundary layer mixing processes: Insights from dye experiments. *Journal of Physical Oceanography*, 37(7), pp.1859-1877.

Charnock, H., 1955. Wind stress on a water surface. *Quarterly Journal of the Royal Meteorological Society*, 81(350), pp.639-640.

Chen, Q., Wang, L., Zhao, H. and Douglass, S.L., 2005a. Prediction of Storm Surges and Wind Waves in Mobile Bay, AL. In *Solutions to Coastal Disasters 2005* (pp. 84-95).

Chen, Q., Zhao, H., Hu, K. and Douglass, S.L., 2005b. Prediction of wind waves in a shallow estuary. *Journal of Waterway, Port, Coastal, and Ocean Engineering*, *131*(4), pp.137-148.

Chen, S.N. and Sanford, L.P., 2009. Axial wind effects on stratification and longitudinal salt transport in an idealized, partially mixed estuary. *Journal of Physical Oceanography*, 39(8), pp.1905-1920.

Churchill, J.H. and Csanady, G.T., 1983. Near-surface measurements of quasi-Lagrangian velocities in open water. *Journal of physical oceanography*, 13(9), pp.1669-1680.

Coogan, J. and Dzwonkowski, B., 2018. Observations of wind forcing effects on estuary length and salinity flux in a river-dominated, microtidal estuary, Mobile Bay, Alabama. *Journal of Physical Oceanography*, 48(8), pp.1787-1802.

Coogan, J., Dzwonkowski, B. and Lehrter, J., 2019. Effects of coastal upwelling and downwelling on hydrographic variability and dissolved oxygen in Mobile Bay. *Journal of Geophysical Research: Oceans*, 124(2), pp.791-806.

Coogan, J., Dzwonkowski, B., Lehrter, J., Park, K. and Collini, R.C., 2021. Observations of dissolved oxygen variability and physical drivers in a shallow highly stratified estuary. *Estuarine, Coastal and Shelf Science*, 259, p.107482.

Coogan, J., Dzwonkowski, B., Park, K. and Webb, B., 2020. Observations of Restratification after a wind mixing event in a shallow highly stratified estuary. *Estuaries and Coasts*, 43(2), pp.272-285.

Du, J., Park, K., Shen, J., Dzwonkowski, B., Yu, X. and Yoon, B.I., 2018. Role of baroclinic processes on flushing characteristics in a highly stratified estuarine system, Mobile Bay,

733 Alabama. *Journal of Geophysical Research: Oceans*, 123(7), pp.4518-4537.
734 https://doi.org/10.1029/2018JC013855, 2018.

735 Dykstra, S.L. and Dzwonkowski, B., 2021. The Role of Intensifying Precipitation on Coastal
736 River Flooding and Compound River-Storm Surge Events, Northeast Gulf of
737 Mexico. *Water Resources Research*, 57(11), p.e2020WR029363.

738 Fairall, C.W., Bradley, E.F., Rogers, D.P., Edson, J.B. and Young, G.S., 1996. Bulk
739 parameterization of air-sea fluxes for tropical ocean-global atmosphere coupled-ocean
740 atmosphere response experiment. *Journal of Geophysical Research: Oceans*, 101(C2),
741 pp.3747-3764.

742 Geyer, W.R., 1997. Influence of wind on dynamics and flushing of shallow
743 estuaries. *Estuarine, coastal and shelf science*, 44(6), pp.713-722.

744 Geyer, W.R. and MacCready, P., 2014. The estuarine circulation. *Annual review of fluid*
745 *mechanics*, *46*, pp.175-197.

746 Goodrich, D.M., Boicourt, W.C., Hamilton, P. and Pritchard, D.W., 1987. Wind-induced
747 destratification in Chesapeake Bay. *Journal of Physical Oceanography*, 17(12), pp.2232-
748 2240.

749 Kato, H. and Phillips, O.M., 1969. On the penetration of a turbulent layer into stratified
750 fluid. *Journal of Fluid Mechanics*, 37(4), pp.643-655.

751 Kim, C.K. and Park, K., 2012. A modeling study of water and salt exchange for a micro-tidal,
752 stratified northern Gulf of Mexico estuary. *Journal of Marine Systems*, 96, pp.103-115.

753 Lange, X. and Burchard, H., 2019. The relative importance of wind straining and
754 gravitational forcing in driving exchange flows in tidally energetic estuaries. *Journal of*
755 *Physical Oceanography*, 49(3), pp.723-736.

756 Li, M., Zhong, L., Boicourt, W.C., Zhang, S. and Zhang, D.L., 2007. Hurricane-induced
757 destratification and restratification in a partially-mixed estuary. *Journal of Marine*
758 *Research*, 65(2), pp.169-192.

759 Li, X., Geyer, W.R., Zhu, J. and Wu, H., 2018. The transformation of salinity variance: A
760 new approach to quantifying the influence of straining and mixing on estuarine
761 stratification. *Journal of Physical Oceanography*, 48(3), pp.607-623.

762 Li, Y. and Li, M., 2011. Effects of winds on stratification and circulation in a partially mixed
763 estuary. *Journal of Geophysical Research: Oceans*, 116(C12).

764 MacCready, P., Geyer, W.R. and Burchard, H., 2018. Estuarine exchange flow is related to
765 mixing through the salinity variance budget. *Journal of Physical Oceanography*, 48(6),
766 pp.1375-1384.

767 Monismith, S., 1986. An experimental study of the upwelling response of stratified reservoirs
768 to surface shear stress. *Journal of Fluid Mechanics*, 171, pp.407-439.

769 NOAA National Geophysical Data Center. 2009: Mobile, Alabama 1/3 arc-second NAVD 88
770 Coastal Digital Elevation Model. NOAA National Centers for Environmental
771 Information. Accessed 2022-01-09. https://www.ncei.noaa.gov/access/metadata/landing-
772 page/bin/iso?id=gov.noaa.ngdc.mgg.dem:671

773 NOAA, 2022: Northern Gulf of Mexico Operational Forecast System (NGOFS2). Latest
774 accessed 3 June 2022, https://tidesandcurrents.noaa.gov/ofs/ngofs2/ngofs.html

775 NOAA, 2022: Tides & Currents Products at East Fowl River Bridge, AL - Station ID:
776 8735523. Latest accessed 3 June 2022,
777 https://tidesandcurrents.noaa.gov/waterlevels.html?id=8735523

778 Noble, M.A., Schroeder, W.W., Wiseman Jr, W.J., Ryan, H.F. and Gelfenbaum, G., 1996.
779 Subtidal circulation patterns in a shallow, highly stratified estuary: Mobile Bay,
780 Alabama. *Journal of Geophysical Research: Oceans*, 101(C11), pp.25689-25703.
781 https://doi.org/10.1029/96JC02506.

782 NORTH AMERICAN REGIONAL REANALYSIS: A long-term, consistent, high-resolution
783 climate dataset for the North American domain, as a major improvement upon the earlier
784 global reanalysis datasets in both resolution and accuracy, Fedor Mesinger et. al,
785 submitted to BAMS 2004.

786 Park, K., Kim, C.K. and Schroeder, W.W., 2007. Temporal variability in summertime bottom
787 hypoxia in shallow areas of Mobile Bay, Alabama. *Estuaries and Coasts*, 30(1), pp.54-65.
788 https://doi.org/10.1007/BF02782967.

789 Park, K., Powers, S.P., Bosarge, G.S. and Jung, H.S., 2014. Plugging the leak: Barrier island
790 restoration following Hurricane Katrina enhances larval retention and improves salinity

791 regime for oysters in Mobile Bay, Alabama. *Marine environmental research*, 94, pp.48-
792 55.

793 Paskyabi, M.B. and Fer, I., 2014. Turbulence structure in the upper ocean: a comparative
794 study of observations and modeling. *Ocean Dynamics*, 64(4), pp.611-631.

795 Purkiani, K., Becherer, J., Klingbeil, K. and Burchard, H., 2016. Wind-induced variability of
796 estuarine circulation in a tidally energetic inlet with curvature. *Journal of Geophysical*
797 *Research: Oceans*, 121(5), pp.3261-3277.

798 Ralston, D.K., Geyer, W.R. and Lerczak, J.A., 2008. Subtidal salinity and velocity in the
799 Hudson River estuary: Observations and modeling. *Journal of Physical*
800 *Oceanography*, 38(4), pp.753-770.

801 Schroeder, W.W., Dinnel, S.P. and Wiseman, W.J., 1990. Salinity stratification in a river-
802 dominated estuary. *Estuaries*, 13(2), pp.145-154. https://doi.org/10.2307/1351583.

803 Scully, M.E., 2016. Mixing of dissolved oxygen in Chesapeake Bay driven by the interaction
804 between wind-driven circulation and estuarine bathymetry. *Journal of Geophysical*
805 *Research: Oceans*, 121(8), pp.5639-5654.

806 Scully, M.E., 2010a. Wind modulation of dissolved oxygen in Chesapeake Bay. *Estuaries*
807 *and coasts*, *33*(5), pp.1164-1175.

808 Scully, M.E., 2010b. The importance of climate variability to wind-driven modulation of
809 hypoxia in Chesapeake Bay. *Journal of Physical Oceanography*, *40*(6), pp.1435-1440.

810 Scully, M.E., Friedrichs, C. and Brubaker, J., 2005. Control of estuarine stratification and
811 mixing by wind-induced straining of the estuarine density field. *Estuaries*, 28(3), pp.321-
812 326.

813 Seim, H.E., Kjerfve, B. and Sneed, J.E., 1987. Tides of Mississippi Sound and the adjacent
814 continental shelf. *Estuarine, Coastal and Shelf Science*, 25(2), pp.143-156.

815 Smolarkiewicz, P.K. and Margolin, L.G., 1998. MPDATA: A finite-difference solver for
816 geophysical flows. *Journal of Computational Physics*, 140(2), pp.459-480.

817 Stacey, M.T., Brennan, M.L., Burau, J.R. and Monismith, S.G., 2010. The tidally averaged
818 momentum balance in a partially and periodically stratified estuary. *Journal of Physical*
819 *Oceanography*, 40(11), pp.2418-2434. https://doi.org/10.1175/2010JPO4389.1.

820 Taylor, P.K. and Yelland, M.J., 2001. The dependence of sea surface roughness on the height
821 and steepness of the waves. *Journal of physical oceanography*, 31(2), pp.572-590.

822 Terray, E.A., Donelan, M.A., Agrawal, Y.C., Drennan, W.M., Kahma, K.K., Williams, A.J.,
823 Hwang, P.A. and Kitaigorodskii, S.A., 1996. Estimates of kinetic energy dissipation
824 under breaking waves. *Journal of Physical Oceanography*, 26(5), pp.792-807.

825 Testa, J.M., Clark, J.B., Dennison, W.C., Donovan, E.C., Fisher, A.W., Ni, W., Parker, M.,
826 Scavia, D., Spitzer, S.E., Waldrop, A.M. and Vargas, V.M., 2017. Ecological forecasting
827 and the science of hypoxia in Chesapeake Bay. *BioScience*, 67(7), pp.614-626.

828 Trowbridge, J.H., 1992. A simple description of the deepening and structure of a stably
829 stratified flow driven by a surface stress. *Journal of Geophysical Research:*
830 *Oceans*, 97(C10), pp.15529-15543.

831 Towns, J, Cockerill, T, Dahan, M, Foster, I, Gaither, K, Grimshaw, A, Hazlewood, V,
832 Lathrop, S, Lifka, D, Peterson, GD, Roskies, R, Scott, JR & Wilkens-Diehr, N 2014,
833 'XSEDE: Accelerating scientific discovery', *Computing in Science and Engineering*, vol.
834 16, no. 5, 6866038, pp. 62-74. https://doi.org/10.1109/MCSE.2014.80

835 Umlauf, L. and Burchard, H., 2003. A generic length-scale equation for geophysical
836 turbulence models. *Journal of Marine Research*, 61(2), pp.235-265.

837 USGS, 2022: USGS Water Data Services of Tombigbee River at Coffeeville L&D NR
838 Coffeeville, AL. Latest accessed 3 June 2022, https://waterdata.usgs.gov/monitoring-
839 location/02469761/#parameterCode=00065&period=P7D

840 USGS, 2022: USGS Water Data Services of Satilpa Creek near Coffeeville, AL. Latest
841 accessed 3 June 2022, https://waterdata.usgs.gov/monitoring-
842 location/02469800/#parameterCode=00060&period=P7D

843 USGS, 2022: USGS Water Data Services of Alabama River at Choctaw Bluff, AL. Latest
844 accessed 3 June 2022, https://waterdata.usgs.gov/monitoring-
845 location/02429540/#parameterCode=00065

846 Wang, D.P., 1979. Wind-driven circulation in the Chesapeake Bay, winter, 1975. *Journal of*
847 *Physical Oceanography*, 9(3), pp.564-572.

848 Wang, T., Geyer, W.R. and MacCready, P., 2017. Total exchange flow, entrainment, and
849 diffusive salt flux in estuaries. *Journal of Physical Oceanography*, 47(5), pp.1205-1220.

Warner, J.C., Sherwood, C.R., Arango, H.G. and Signell, R.P., 2005. Performance of four turbulence closure models implemented using a generic length scale method. *Ocean Modelling*, 8(1-2), pp.81-113.

Weisberg, R.H., 1976. The Noutidal flow in the Providence River of Narragansett Bay: A stochastic approach to estuarine circulation. *Journal of Physical Oceanography*, 6(5), pp.721-734.

Wei, E., Zhang, A., Yang, Z., Chen, Y., Kelley, J.G., Aikman, F. and Cao, D., 2014. NOAA's Nested Northern Gulf of Mexico operational forecast systems development. *Journal of Marine Science and Engineering*, 2(1), pp.1-17.

Wilmott, C., 1., 1981. On the validation of models. *Phys. Georgr*, pp.2-184.

Wong, K.C. and Garvine, R.W., 1984. Observations of wind-induced, subtidal variability in the Delaware Estuary. *Journal of Geophysical Research: Oceans*, 89(C6), pp.10589-10597.

Wong, K.C. and Moses-Hall, J.E., 1998. On the relative importance of the remote and local wind effects to the subtidal variability in a coastal plain estuary. *Journal of Geophysical Research: Oceans*, 103(C9), pp.18393-18404.

Wong, K.C. and Valle-Levinson, A., 2002. On the relative importance of the remote and local wind effects on the subtidal exchange at the entrance to the Chesapeake Bay. *Journal of Marine Research*, 60(3), pp.477-498.

Zhang, W., Wu, H., Hetland, R.D. and Zhu, Z., 2019. On mechanisms controlling the seasonal hypoxia hot spots off the Changjiang River Estuary. *Journal of Geophysical Research: Oceans*, 124(12), pp.8683-8700.

Zheng, L., Yang, Z., Lindley, C. and Myers III, E.P., 2020, December. NOAA/NOS Integrated Northern Gulf of Mexico Operational Forecast System. In *AGU Fall Meeting Abstracts* (Vol. 2020, pp. OS002-0009).